Toward DLP 4D printing of liquid crystal elastomers: Tailored properties via non-mesogenic linkers

Rakine Mouhoubi, Philippe Dieudonné-Georges, Olivier Arnould, Vincent Lapinte, Sébastien Blanquer

Toward DLP 4D Printing of Liquid Crystal Elastomers: Tailored Properties *via* Non-Mesogenic Linkers

Rakine Mouhoubi[a], *Philippe Dieudonné-Georges*[b], *Olivier Arnould*[c], *Vincent Lapinte*[a], *Sébastien Blanquer*[a*]

[a]Institut Charles Gerhardt Montpellier (ICGM), CNRS, Université de Montpellier, ENSCM, Montpellier, France

[b]Laboratoire Charles Coulomb (L2C), CNRS, Université de Montpellier, France

[c]Laboratoire de Mécanique et Génie Civil (LMGC), CNRS, Université de Montpellier, France

E-mail: sebastien.blanquer@umontpellier.fr

ABSTRACT:

Three-dimensional printing of soft actuators offers a great potential for creating flexible and adaptable structures in diverse applications such as artificial muscles, medical devices and soft robots. Digital light processing (DLP) is particularly effective in fabricating complex 3D structures with high resolution. Here we present an approach to DLP 3D print liquid crystal elastomers (LCEs) with controlled properties by incorporating non-mesogenic linkers. By varying the length of these linkers, the thermo-mechanical properties, including the nematic-isotropic transition temperature (90 to 36 °C) and the elastic modulus (1 to 57 MPa), can be fine-tuned. The potential of this method is shown by DLP 3D printing LCE structures that exhibit tunable shape recovery behaviour. This approach paves the way of 4D printing technology and enhances the capabilities of 3D-printed soft actuators to meet the requirements of specific applications.

KEYWORDS: soft actuators; liquid crystal elastomers; non-mesogenic linkers; Digital Light Processing; 3D printing; shape-memory.

Graphical Abstract

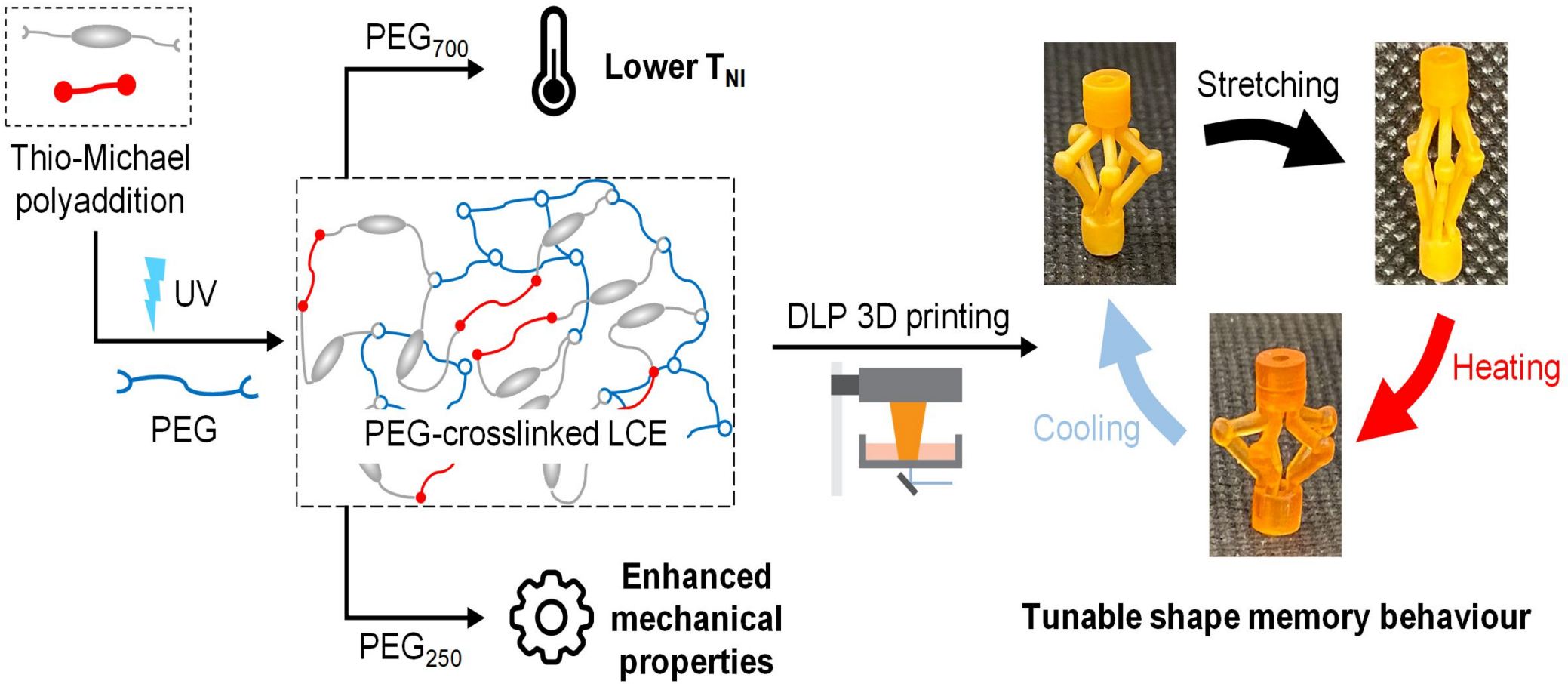

INTRODUCTION

Soft actuators offer many advantages over conventional hard actuators, such as flexibility, adaptability and reconfigurability, inspired by living systems.[1] They generally incorporate smart soft materials capable of changing shape and/or properties under the influence of external stimuli.[2] These characteristics have enabled soft actuators to be used in a wide range of applications such as artificial muscles,[3] soft grippers,[4] medical, haptic and wearable devices[5] and soft robots[6]. However, traditional manufacturing techniques as molding and casting are not able to meet the growing demands for sophisticated architectures.[7] New functional materials and fabrication methods have therefore been developped for soft actuators to address these needs. Among these methods, additive manufacturing techniques offer a simple and rapid approach to create soft actuators with complex 3D structures. In particular, combining additive manufacturing and stimuli-responisve soft materials leads to 4D printing. This emerging technology enables 4D printed structures to be programmed to change their shape, properties or functions over time in response to an external stimulus.[8] Among 4D printable soft smart materials, shape-memory polymers,[9–11] hydrogels[12–14] and liquid crystal elastomers (LCE)[15–20] have attracted increasing interest because of their versatile properties and responsiveness.

LCEs are particularly attractive as they can undergo a large, rapid and reversible actuation *via* a nematic-isotropic phase transition when exposed to external stimuli such as heat, light, or solvent.[21] Compared to soft smart polymers such as hydrogels which have slower response times, LCEs stand out as being suitable for applications requiring fast actuation.[22] They combine anisotropic properties provided by the orientational order of liquid crystal (LC) molecules called mesogens and entropic elasticity properties due to a lightly crosslinked polymer network. The temperature at which this reversible phase transition occurs is the nematic-isotropic transition temperature (T_{NI}). When heating above the T_{NI}, the aligned

mesogenic units lose their original orientation and become randomly arranged. This then induces a major change in the conformation of the polymer chains, leading to a significant change in the shape of the LCE in the direction of mesogen alignment.[21]

Printing techniques have therefore been developed to exploit the unique properties of LCEs in complex architectures. These include extrusion-based methods such as direct ink writing (DIW)[16,17,23–30] and fused deposition modeling (FDM),[31] vat photopolymerization techniques like digital light processing (DLP)[15,32–36] and laser stereolithography,[37] as well as inkjet printing[17]. Extrusion-based methods, in particular DIW, are commonly used because they have the advantage of enabling shear-induced mesogen alignment during the printing. However, these techniques have a low resolution limited by the nozzle diameter and the viscosity of the ink. Vat photopolymerisation is therefore a promising alternative, particularly DLP which offers a fast printing speed and precision while maintaining a high resolution.[19] It enables 3D objects with complex structures to be printed by photocrosslinking successive layers of a liquid or viscous prepolymer.

Unfortunately, DLP-printed LCEs have two main drawbacks. One one hand, they have a relatively high T_{NI}, typically above 70 °C for standard LCEs derived from photopolymerisable acrylate-terminated inks.[38] For now, only a few studies have reported T_{NI} at lower temperatures. A method has been explored to achieve customizable T_{NI} using various mesogens and spacers. However, this approach relies on the thiol-ene photopolymerization of thiol-terminated inks, which exhibits low reactivity and requires relatively high UV power.[16,38] In addition, the availability of various types of diacrylate mesogens with distinct mesogenic cores is limited, making it difficult to tailor the T_{NI} only by changing the nature of the mesogens.[39] Consequently, other studies have also investigated substituting some of the mesogens with non-mesogenic linkers to achieve low T_{NI}.[40,41] However, none of them is yet

adapted to DLP inks for LCE synthesis. On the other hand, LCEs lack mechanical strength compared to the other actuators such as high-modulus nitinol shape memory alloy. Some studies have suggested semi-crystalline LCE systems that exhibit high modulus by varying the length of alkyl spacers.[42,43] Another developed interpenetrating polymer networks using an acrylate LCE network and a second polyurethane network. However, these systems have very high T_{NI} above 80 °C.

Herein, we introduce a new approach to tailor LCE properties by incorporating non-mesogenic linkers directly into the network. This method is straightforward and compatible with DLP 3D printing. By varying the length of these non-mesogenic linkers, the properties of LCEs can be fine-tuned, providing a high degree of control over their thermo-mechanical properties. First, LCEs are synthesised from liquid crystal oligomers (LCO) of different lengths. The impact of adding non-mesogenic linkers on the thermo-mechanical and mechanical properties, as well as the shape recovery behavior of the resulting LCE networks, is then assessed. The observed changes are supported by wide angle X-ray scattering (WAXS) showing how these linkers affect the LC order. Furthermore, the potential of this approach for 4D printing is demonstrated by fabricating artificial muscle-like structures and stickmen as shape-memory soft actuators with tunable shape recovery behaviour.

MATERIALS AND METHODS

Chemicals

1,4-Bis[4-(3-acryloyloxypropyloxy)benzoyloxy]-2-methylbenzene (≥ 95%, RM257) was purchased from Smolecule (San Antonio, USA). 2,2-(Ethylenedioxy)diethanethiol (≥ 95%, EDDET), 2,6-di-tert-butyl-4-methylphenol (≥ 99%, BHT), Orange G, phenylbis(2,4,6-trimethylbenzoyl)phosphine oxide (≥ 97%, PPO) and poly(ethylene glycol) diacrylate average M_n 250 and 700 g/mol (PEG_{250} and PEG_{700}) were purchased from Sigma Aldrich (France).

Triethylamine (≥ 99%, TEA) was purchased from Carlo Erba (France). Propylene carbonate (≥ 99%) was purchased from Thermoscientific (France). All materials were used as-received without further purification.

Synthesis of LCOs

To synthesise LCOs with different degrees of polymerisation (DP_n), RM257 and EDDET were combined in molar ratios of 1.08:1, 1.15:1, 1.25:1 and 1.35:1. A 1:2 wt% ratio of RM257 and propylene carbonate was added to a 25 mL vial along with BHT (2 wt%) and PPO (2 wt%). The vial was then heated at 85 °C, vortex-mixed and allowed to cool at room temperature before adding EDDET. Subsequently, the resulting isotropic mixture was vortex-mixed and a 10 wt% solution of TEA (9 mol%) in propylene carbonate was added dropwise to initiate the polymerisation. After the vial was vortex-mixed, the reaction was allowed to proceed for 16 h at room temperature. The resulting LCO ink was used without further purification.

The LCOs were labelled "LCO*x*", *x* being the degree of polymerization (DP_n) value determined by ^{1}H NMR spectroscopy.

Synthesis of LCEs

To synthesize standard LCEs, the LCO inks were directly poured in a PTFE mould and photo-crosslinked under a 365 nm UV light (20 mW/cm^2) for 20 min using UV Crosslinker Bio-Link chamber (Thermo Fisher, France). The obtained samples were washed by swelling in toluene for 48 h to remove unreacted polymer residues and dried in a vacuum oven at 90 °C for 24 h.

To synthesise PEG_{250}-crosslinked LCEs, LCO inks and PEG_{250} were combined so that the mole fraction of acrylate functional groups contributed by PEG_{250} to the network was studied at 20, 25 and 45 mol%. The LCO inks and PEG_{250} were vigorously vortex-mixed for uniform mixing. Afterwards, the samples were photo-crosslinked and washed using the same decribed procedure.

To synthesise PEG_{700}-crosslinked LCEs, LCO inks and PEG_{700} were combined so that the mole fraction of acrylate functional groups contributed by PEG_{700} to the network was studied at 10, 20 and 25 mol%. The LCO inks and PEG_{700} were vigorously vortex-mixed for uniform mixing. Afterwards, the samples were photo-crosslinked and washed using the same decribed procedure.

The LCEs were labelled "LCE*x*", *x* being the DP_n of the LCO precursor–"PEG_nz", *n* being the M_n value of the PEG diacrylate used and *z* being by the mole fraction of acrylate functional groups contributed by the non-mesogenic linker to the network.

To synthesise crosslinked-PEG_{250}, a 1:2 wt% ratio of PEG_{250} and propylene carbonate was added to a 25 mL vial along with BHT (2 wt%) and PPO (2 wt%). The vial was then vortex-mixed for uniform mixing. Afterwards, the samples were photo-crosslinked and washed using the same decribed procedure. The same method was used to synthesise crosslinked-PEG_{700}.

^{1}H NMR characterization

^{1}H NMR spectroscopy was employed to determine the DP_n and the number-average molecular weights (M_n) of the LCOs through end-group detection. The ^{1}H NMR spectra were realised using a 400 MHz Bruker's Avance Spectrometer with $CDCl_3$ as deuterated solvent. The chemical shifts of protons were relative to $CHCl_3$ residual in $CDCl_3$ at $\delta = 7.26$ ppm. The DP_n and M_n values for each LCO were calculated based on the ratio of six protons in the diacrylate end-groups to four aromatic protons in the repetitive mesogen unit using the following equations eq. 1. and eq. 2.:

$$\mathrm{DP}_{n,NMR} = \frac{\frac{\int_{8}^{8.15} I}{4}}{\frac{\int_{5.7}^{5.85} I + \int_{6}^{6.15} I + \int_{6.3}^{6.4} I}{6}} - 1 \qquad (1)$$

$$M_{n,NMR} = DP_{n,NMR} \times M_{repeating\ unit} + M_{end-groups} \quad (2)$$

where $M_{repeating\ unit}$ and $M_{end\text{-}groups}$ are the molar masses of the repeating unit ($M_{repeating\ unit}$ = 772 g/mol) and the end groups ($M_{end\text{-}groups}$ = 588 g/mol) respectively.

Size exclusion chromatography

Size exclusion chromatography (SEC) was used to determine the molecular weight distribution of the LCOs. The LCO inks were first precipitated in ethanol and the resulting LCOs were dried in an oven at 80 °C for 24 h. SEC measurements were performed on a Varian 390-LC apparatus with a refractive index detector from Agilent Technologies, equipped with two columns Infinitylab Oligopore. The eluent was DMF containing 0.1 wt% LiCl, with a flow rate of 0.8 mL/min at 40 °C. Samples were filtered using AIT France PTFE syringe filters (0.22 µm, 13 mm diameter) before the injection. Linear poly(methyl methacrylate)s (PMMA) were used as standards. The curves were normalized to maximum intensity.

Differential scanning calorimetry

Differential scanning calorimetry (DSC) was used to evaluate the thermal properties of the LCOs. DSC analyses were carried out using a Netzsch DSC 3500 Sirius. The ethanol-precipitated and dried LCOs with a mass between 5 and 10 mg were loaded into standard aluminum DSC pans. The samples were equilibrated at -50 °C and heated to 120 °C at a rate of 10 °C/min. They were then cooled slowly to -50 °C at a rate of 2 °C/min to allow LC self-assembly. They were then heated to 120 °C at a rate of 20 °C/min. Data were reported from the second heating scans. The glass transition temperature (Tg) was defined at the step change in the slope of the heat flow signal. The nematic-isotropic transition temperature (T_{NI}) was determined at the minimum value of the endothermic peak. The enthalpy change (ΔH_{NI}) was measured by integrating the endothermic energy well of the nematic-isotropic transition. The

same method was also used to characterise the Tg of crosslinked-PEG_{250} and crosslinked-PEG_{700} materials.

Dynamic mechanical analysis

Dynamic mechanical analysis (DMA) was employed to study the thermo-mechanical properties and the phase transitions of the LCEs. DMA tests were performed using a Mettler Toledo DMA instrument. Rectangular samples measuring approximately 20 x 1 x 1 mm^3 were tested in tensile mode, with an active length of 10 mm. The samples were equilibrated at -50 °C. They were then subjected to a strain of 0.2% at 1 Hz and heated from -50 to 120 °C at a rate of 2 °C/min. Tg was defined at the maximum value of the loss tangent (tan δ) curve. T_{NI} was attributed to the lowest value of the storage modulus (E') curve above Tg. The nematic modulus (E'_n) and isotropic modulus (E'_i) were measured using the storage modulus values at 25 °C and T_{NI} + 20 °C, respectively.

Uniaxial tensile testing

Uniaxial tensile tests were performed to study the mechanical properties of PEG_{250}-crosslinked LCE5 and PEG_{700}-crosslinked LCE5. The tensile tests were executed on an Instron 3366L5885 mechanical tester equipped with a 100 N load cell. Rectangular samples measuring approximately 20 x 1 x 1 mm^3 were tested at a displacement rate of 5 mm/s. The Young modulus was measured by taking the slope in the linear region of the stress-strain curve between 0 and 0.5% strain. The threshold stress was determined as the stress at the intersection of the tangents of the first linear region and the soft elasticity plateau. The failure strain value was defined as the maximum strain at break.

Strain recovery testing

The strain recovery and strain fixity of PEG_{250}-crosslinked LCE5 and PEG_{700}-crosslinked LCE5 were monitored using a TA (formerly Bose) Electroforce 3230 instrument equipped with a 22 N load cell, a ±6 mm displacement sensor and a hot/cold chamber. Rectangular samples

measuring approximately 20 x 1 x 1 mm^3 were tested in tensile mode, with an active length of 10 mm. The samples were strained at a rate of 10 %/min at around 25 °C until they reached 100% engineering strain. The stress was then immediately relaxed to 0.01 N. The samples were then allowed to exhibit free-standing recovery for 10 min until the engineering strain had stabilized. Finally, the samples were heated to 120 °C at a rate of 0.07 °C/s. The strain fixity (R_f) was calculated using the following equation:

$$R_f = \frac{\varepsilon_{free-standing\ recovery}}{\varepsilon_{max}} \times 100 \quad (3)$$

where $\varepsilon_{\text{free-standing recovery}}$ is the free-standing recovery engineering strain after 10 min at 0.01 N and ε_{max} is the maximum engineering strain to which the samples were subjected (ε_{max} = 100%).

The stress at maximum strain was defined as the stress value at ε_{max} = 100%. The maximum recovery temperature was determined as the temperature value for which the first derivative of the engineering strain as a function of temperature was maximum. The clamp thermal expansion correction was applied with a coefficient of 0.01 mm/°C measured without sample in the same temperature range.

Polarised optical microscopy

Polarised optical microscopy (POM) was used to investigate the presence of LC order for PEG_{250}-crosslinked LCE5 and PEG_{700}-crosslinked LCE5. An optical microscope Leica DM 6000M coupled to a camera and equipped with a cross polariser-analyser was used. The samples were held between the polariser and the analyser and were imaged with the light transmitted through them. The objective used was x50.

Wide angle X-ray scattering

Wide angle X-ray scattering (WAXS) was employed to measure the orientational order of the LC phase for LCE5-PEG_{250} and LCE5-PEG_{700} as a function of temperature. The experiments were performed with an in-house setup. A high brightness low power X-ray tube, coupled with

an aspheric multilayer optic (GeniX3D from Xenocs) was employed. It delivered an ultralow divergent beam (0.5 mrad, λ=0.15418 nm). Scatterless slits were used to give a clean 0.6 mm beam diameter with a flux of 35 Mphotons/s at the sample. A transmission configuration was used and the scattered intensity was measured by a 2D "Pilatus" 300 K pixel detector by Dectris (490*600 pixels) with a pixel size of 172×172 μm^2, at a distance of 100 mm from the sample for WAXS configuration. The order parameter (S) was calculated using the following equation eq. 4. :

$$S = \frac{\int_0^{\pi/2} I(\theta) \frac{3cos^2\theta - 1}{2} sin\theta d\theta}{-\frac{1}{2}\int_0^{\pi/2} I(\theta) sin\theta d\theta} \quad (4)$$

where θ is the angle between the director and mesogenic units and I(θ) is the azimuthal intensity distribution. The calculation was carried out for θ between 0 and 90 °.

Fabrication of DLP 3D printed structures

Two ink formulations were prepared for DLP 3D printing. For the first ink formulation, LCO5 ink was vigorously vortex-mixed with Orange G (0.2 wt% relative to the ink without solvent) as a colouring agent to provide an efficient cure depth and an optimal pattern resolution. For the second ink formulation, LCO5 and PEG_{700} were combined so that 10 mol% of acrylate functional groups were contributed by PEG_{700} to the network. LCO5 ink and PEG_{700} were rigorously vortex-mixed with Orange G (0.2 wt% relative to the ink without solvent).

3D models were designed using the software Rhinoceros 3D and exported as STL files. The 3D structures were then built from the mentioned inks by stereolithography using a commercial Asiga Max X43 machine (KREOS supplier, France) with an integrated 385 nm LED and a pixel resolution of 43 μm.

The ideal layer thickness was fixed at 100 μm. The optimum irradiation time was determined using Jacob's equation[44] by measuring the generated curing depths at 1.13 mW/cm². For a

layer thickness of 100 µm, each layer was irradiated at 1.13 mW/cm² for 10 and 9.4 s, for the first and second ink formulations respectively. After construction, the structures were swelled in toluene for 48 h and dried in a vacuum oven at 90 °C for 24 h.

To demonstrate the shape-recovey behaviour of the 3D printed LCEs, the structures were stretched to 100% engineering strain. They were then maintained at a temporary shape after unloading. R_f was calculated using eq. 3 after image processing on ImageJ.

RESULTS AND DISCUSSION

LCEs from different LCO precursors

The impact of LCO length on the properties of the resulting LCEs was first studied. The LCOs were synthesised from a mesogenic diacrylate (RM257) and an isotropic dithiol (EDDET) *via* a base-catalysed thiol-Michael polyaddition in propylene carbonate, as illustrated in Figure 1a. Propylene carbonate was initially chosen over other solvents like toluene and dichloromethane usually used in 3D printing of LCEs due to its lower toxicity, reduced environmental impact and lower volatility[45]. A molar excess of RM257 over EDDET was chosen to obtain acrylate-terminated LCOs (Figure 1b). Different molar ratios were employed to target DP_n calculated theoretically by Carothers equation.[46] The obtained LCOs were characterised by ^{1}H NMR to determine the DP_n (with one unit represented in Figure 1b) and the M_n through end-group detection, as detailed in the Materials and Methods section. The values are listed in Table 1 and the ^{1}H NMR spectra are provided in Figure S1. The LCOs are labelled "LCO*x*", *x* being the DP_n value determined by ^{1}H NMR spectroscopy. The resulting DP_n values are lower than theoretically predicted, potentially due to the presence of impurities, although the overall trend remains consistent. As expected, increasing the molar amount of RM257, which deviates further from the stoichiometric ratio, leads to a decrease in DP_n. This trend was also confirmed by SEC, as shown in Figure 1c. The broad SEC traces also indicate a wide range of molecular weights, which is characteristic of a step-growth polymerisation. As can be seen in Table 1, the

polydispersity index (Đ) of LCOs increases as the molar amount of RM257 decreases, confirming that achieving a higher DP_n results in higher polydispersity. Since the DP_n is expected to influence the phase behaviour, the LCOs were then characterised by DSC (Figure 1d). The values of transition temperature and associated enthalpy change are listed in Table 1. Although there is no significant change in Tg, the LCOs exhibit a drop in T_{NI} from 85 to 69 °C with associated enthalpy values also decreasing as the DP_n increases from 5 to 16. The observed decrease in T_{NI} can be attributed to enhanced chain mobility and higher entropy leading to weaker π–π stacking interactions as evidenced by the lower enthalpy changes.

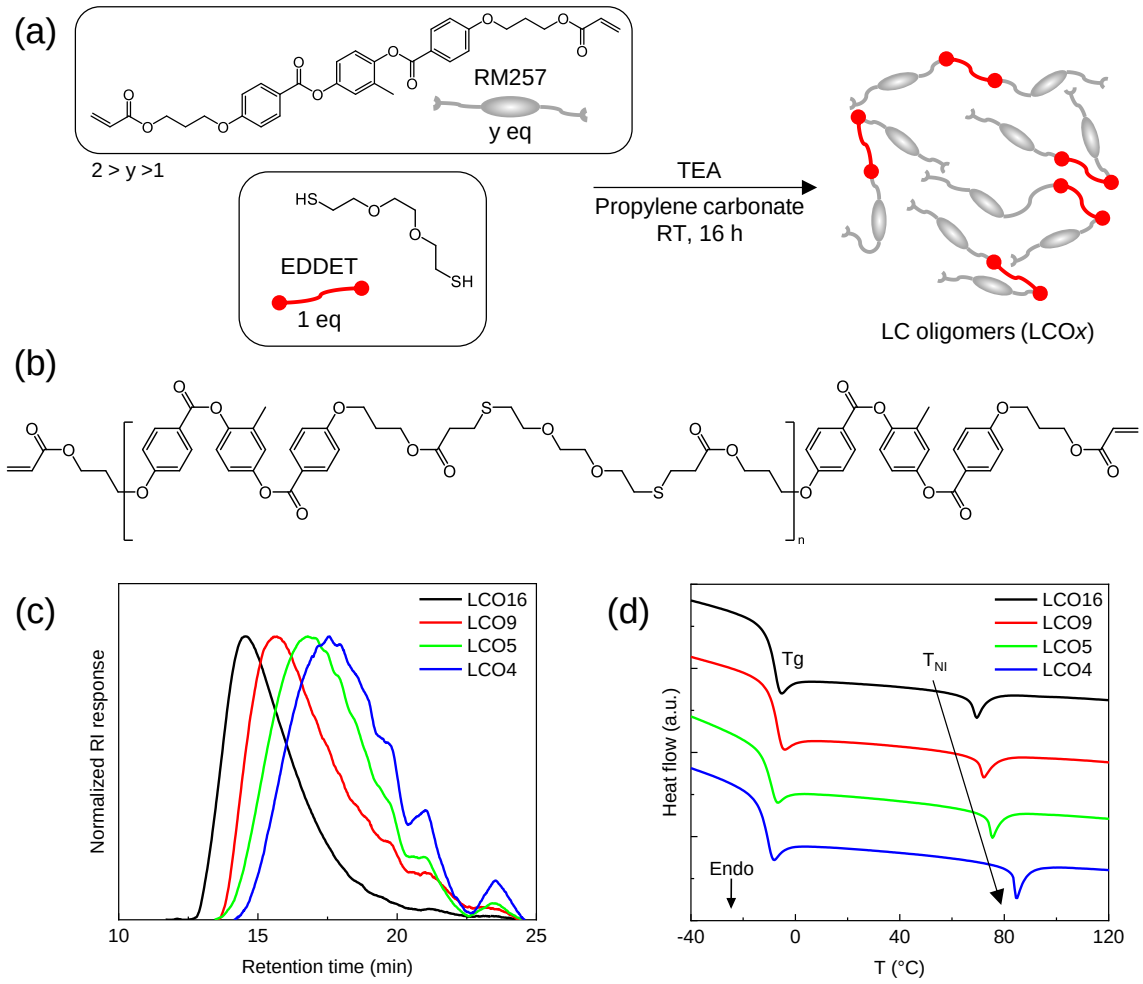

Figure 1: (a) Reaction scheme illustrating the LCO synthesis *via* the thiol-Michael polyaddition reaction. LCOs are labelled "LCO*x*", *x* being the DP_n value determined by ^1H

NMR spectroscopy. (b) Chemical structure of the resulting acrylate-terminated LCO. (c) SEC traces of the LCOs synthesised with varying RM257:EDDET molar ratios. (d) DSC traces of these LCOs.

Table 1: Summary of ^{1}H NMR and DSC data for LCO characterisation.

	Molar ratio RM257:EDDET	DP_n[a] calc.	M_n calc.[b] (g/mol)	DP_n[c] theo.	Đ[d]	Tg[e] (°C)	T_{NI}[e] (°C)	ΔH_{NI}[e] (J/g)
LCO4	1.35:1	4	3676	7	3.5	-13	85	1.64
LCO5	1.25:1	5	4448	9	4.0	-11	75	1.55
LCO9	1.15:1	9	7536	14	5.9	-9	72	1.49
LCO16	1.08:1	16	12940	26	7.9	-8	69	1.33

[a] Calculated according to eq 1 from ^{1}H NMR spectra. [b] Calculated according to eq 2 from ^{1}H NMR spectra. [c] Calculated according to Carother's equation[46]. [d] Determined by SEC. [e] Determined by DSC.

The LCOs were subsequently photo-crosslinked into LCEs through the homopolymerisation of excess acrylates under UV light, as illustrated in Figure 2a. The LCEs are labelled "LCE*x*", *x* being the DP_n value of the LCO precursor. These LCE networks exhibited a high gel fraction of over 94% (Figure S2), indicating an efficient crosslinking. DMA was first performed on these LCEs to study the evolution of their thermo-mechanical properties as a function of the DP_n of the LCO precursors. The DMA traces of LCEs are shown in Figure 2b. The values of transition temperature and storage modulus are listed in Table 2. Overall, the LCEs all exhibit a dynamic soft elastic behaviour characterized by a broad tan δ curve between the Tg and the T_{NI} along with a temporary drop in E' at the T_{NI}. More specifically, a decrease in T_{NI} from 96

to 71 °C is observed when the DP_n of the LCO precursors increases from 5 to 16. This is because increasing the DP_n of LCOs leads to longer chain segments between crosslinks. As a result, these longer segments enhance mobility and lead to an increase in entropy. Additionally, there are less mesogens in the network leading to fewer π–π stacking interactions. These factors collectively disrupt the nematic order, thereby reducing the T_{NI}. Furthermore, increasing the DP_n of LCO precursors results in a decrease in Tg from 12 to -1 °C and a reduction in E'_n for the resulting LCEs. This is due to a lower crosslinking density and an increased chain mobility that contribute to making the material more flexible. Then, to better understand the mechanical properties of these LCEs under static loading conditions, tensile tests were carried out, as shown in Figure 2c. The values of Young modulus, threshold stress (*i.e.*, the stress at which the soft elasticity region, characterised by a nearly constant stress, is initiated) and failure strain are listed in Table 2. As expected, as the DP_n of LCO precursors increases, the resulting LCEs exhibit greater flexibility and less stiffness, allowing them to deform further before failure, up to a strain of over 900% for LCE16. The soft elastic behaviour is also strongly influenced by the DP_n of the LCO precursors. For instance, the soft elasticity region for LCE5 is between 30 and 80% strain with a threshold stress of around 200 kPa. When the DP_n of LCO precursors increases, the soft elasticity region extends and the threshold stress decreases. For example, LCE16 demonstrates a soft elasticity region between 10 and 100% strain with a threshold stress of around 16 kPa. This can be attributed to a lower crosslinking density. Consequently, it requires less stress to initiate mesogen and anisotropic polymer chain conformation orientation along the loading axis. Furthermore, a wider region of soft elasticity is achieved as the material is more flexible. It can also be seen that LCE4 has a very restricted region of soft elasticity, with a behaviour approaching that of a liquid crystal network (LCN). In general, the properties of these LCEs are equivalent to those of LCEs synthesized more conventionally in the literature, in terms of Tg, T_{NI}, E'_n, failure strain and threshold stress.[47–49]

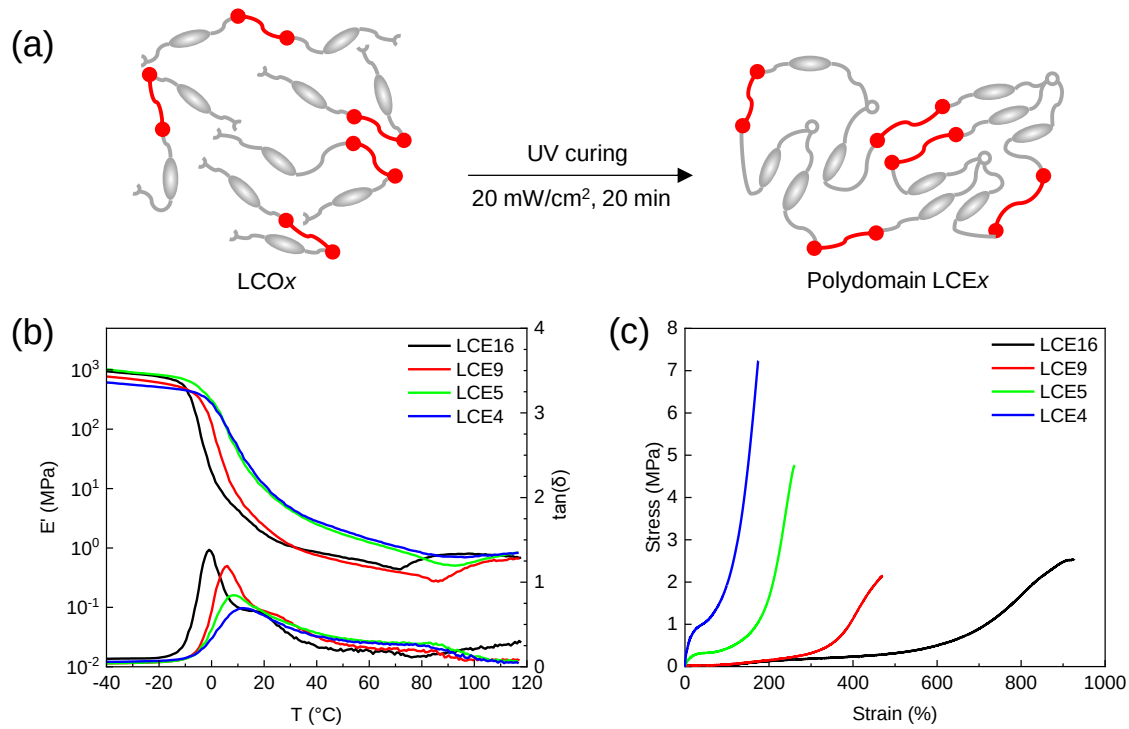

Figure 2: (a) Reaction scheme illustrating the LCE synthesis. LCEs are labelled "LCE*x*", *x* being the DP_n value of the LCO precursor. (b) Storage modulus (E') and loss tangent (tan δ) traces of LCEs. (c) Stress–strain curves of LCEs.

Table 2: Summary of DMA and tensile test data for LCE characterization.

	Tg[a] (°C)	T_{NI}[a] (°C)	E'$_n$[a] (MPa)	E'$_i$[a] (MPa)	Young modulus[b] (MPa)	Threshold stress[b] (kPa)	Failure strain[b] (%)
LCE4	12	96	7.0	0.8	19.7 ± 1.1	533.8 ± 8.6	181.9 ± 8.3
LCE5	9	93	6.3	0.8	4.2 ± 0.6	206.7 ± 3.4	259.5 ± 20.9
LCE9	6	86	1.6	0.6	1.2 ± 0.1	29.8 ± 6.5	459.6 ± 17.4
LCE16	-1	71	1.3	0.8	0.6 ± 0.1	16.0 ± 0.7	971.6 ± 42.6

[a] Determined by DMA. [b] Determined by uniaxial tensile testing.

Influence of non-mesogenic linkers

The influence of adding of non-mesogenic linkers on the properties of the resulting LCEs was then studied. PEG diacrylate was chosen as a non-mesogenic linker because of its similar chemical structure to EDDET with inert ether bonds. Two different PEG chain lengths were selected, namely PEG_{250} and PEG_{700}. As illustrated in Figure 3a, they were combined to LCO with a fixed DP_n and the resin was further photo-crosslinked into LCEs under UV light. The synthesised LCEs are labelled "LCE*x*", *x* being the DP_n of the LCO precursor–"PEG_nz", *n* being the M_n value of the PEG diacrylate used and *z* being by the mole fraction of acrylate functional groups contributed by the non-mesogenic linker to the network. PEG_{250} and PEG_{700} were chosen because of the major differences in their polymer network properties when photo-crosslinked. Specifically, crosslinked-PEG_{700} has a Tg of -38 °C, which corresponds to a rubbery state at room temperature, while crosslinked-PEG_{250} has a Tg of 36 °C, which corresponds to a glassy state at room temperature (Figure S3). Thus, for LCEs with a Tg between -1 and 12 °C, PEG_{250} acts as a network hardener while PEG_{700} acts as a network softener. DMA was therefore performed to monitor the evolution of thermo-mechanical properties of the LCEs as a function of the mole fraction of acrylate functional groups contributed by the non-mesogenic linker used to the network. The DMA traces are shown in Figures 4a and 4b for PEG_{700}-crosslinked LCE5 and the rest of the spectra are shown in Figures S4-S7. The changes in Tg and T_{NI} with the addition of PEG_{250} and PEG_{700} are shown in Figure 3b and Figure 3c, respectively. The changes in E'_n are plotted in Figure S8. First, when LCO16 is combined with the two non-mesogenic linkers, no significant influence is observed on both Tg and T_{NI}. Indeed, even if the crosslinking density is increased by the addition of PEG diacrylates, the segments between crosslinks are sufficiently long to maintain their mobility and preserve the nematic order. However, as the DP_n of the LCOs decreases, the impact of PEG_{250} and PEG_{700} on the transition temperatures becomes more pronounced. Specifically, increasing the molar content of PEG_{250} in the network leads to a notable increase in the Tg,

resulting in a stiffer material with E'_n reaching, for example, 57 MPa for LCE5-PEG_{250}45 (Table 3). Conversely, the addition of PEG_{700} causes a slight decrease in Tg, making the material slightly softer with E'_n values within the range of typical LCEs[47]. Regarding the T_{NI}, the length of the PEG diacrylate chain plays a critical role. Increasing the molar content of PEG_{250} causes a slight decrease in T_{NI} until a threshold is reached. However, increasing the molar content of PEG_{700} leads to a significant decrease in T_{NI}. For instance, the T_{NI} for LCE5-PEG_{250}25 is 66 °C, whereas for the same crosslinking density, the T_{NI} drops to 36 °C for LCE5-PEG_{700}25 (Table 3). Previous studies have shown that T_{NI} of LCEs varies linearly with the LC mass content in the polymer network and is much less dependent on mesogen, crosslinking density, linker composition, network genesis or chemistry[50]. But here, as illustrated in Figure S9, for similar LC mass content, the T_{NI} differs markedly with the addition of PEG_{700} compared to PEG_{250}. Therefore, the length of the non-mesogenic linker is also a key parameter influencing the nematic order and, consequently, the T_{NI}.

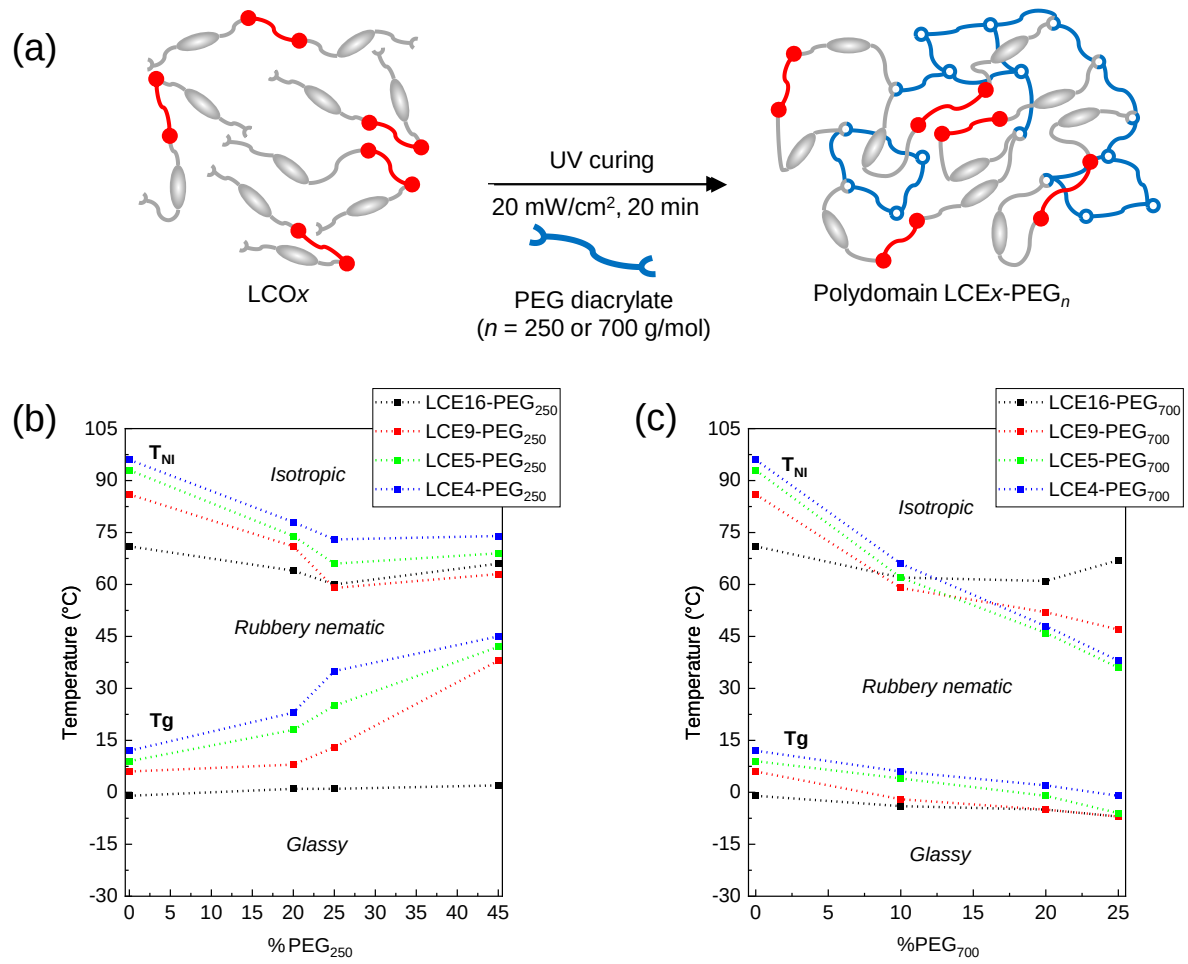

Figure 3: (a) Reaction scheme illustrating the PEG-crosslinked LCE synthesis. LCEs are labelled "LCE*x*", *x* being the DP_n value of the LCO precursor–"PEG*n*", *n* being the M_n value of the PEG diacrylate used. (b) Transition temperatures Tg and T_{NI} of LCE*x*-PEG_{250} as a function of the mole fraction of acrylate functional groups contributed by PEG_{250} to the network. (c) Transition temperatures Tg and T_{NI} of LCE*x*-PEG_{700} as a function of the mole fraction of acrylate functional groups contributed by PEG_{700} to the network. The dashed lines are guide to the eye.

PEG_{250}-crosslinked LCE5 and PEG_{700}-crosslinked LCE5 were further examined due to their significant differences in thermo-mechanical properties while still exhibiting the characteristic LCE behaviour. Uniaxial tensile tests were conducted to assess the mechanical properties of these networks. The stress-strain curves for PEG_{700}-crosslinked LCE5 are presented in Figure

4b, and those for PEG_{250}-crosslinked LCE5 are shown in Figure S10. The values of Young modulus, threshold stress, and failure strain are listed in Table 3. First, as the molar content of PEG_{250} increases, the material becomes stiffer and the failure strain slightly decreases, remaining above 200% despite the increased crosslinking density. In contrast, increasing the molar content of PEG_{700} results in a softer material with a significant decrease in failure strain, from around 200% for LCE5-PEG_{700}10 to around 60% for LCE5-PEG_{700}25. Furthermore, for both PEG_{250} and PEG_{700}, the addition of non-mesogenic linkers results in a restricted region of soft elasticity, with this effect being more significant for PEG_{700}-crosslinked LCE5. This pronounced reduction in strain and soft elasticity region can be attributed to the greater disruption of the LC domains by PEG_{700} compared to PEG_{250}. This disruption hinders the reorientation of the LC domains under applied stress, thereby reducing the overall strain the material can achieve and the phenomenon soft elasticity region. Strain recovery tests were then conducted to compare the ability of PEG_{250}-crosslinked LCE5 and PEG_{700}-crosslinked LCE5 networks to retain a temporary strain upon unloading and to recover their original shape upon heating (Figure 4c). The samples were first strained to 100% engineering strain and then unloaded to 0.01 N. Strain fixity (R_f) was measured after a 10 min isothermal hold at constant load, which was the optimal time for which a plateau of temporary strain retained was observed. Then the samples were heated to 120 °C to induce strain recovery. LCE5-PEG_{250}45 and LCE5-PEG_{700}25 were not included in this study because their network properties closely approach those of LCNs. The values of R_f, stress at maximum strain and maximum recovery temperature (i.e., the temperature at which the first derivative of engineering strain as a function of temperature was maximal) are listed in Table 4. First, R_f decreases with the addition of non-mesogenic linkers. The effect is more pronounced for PEG_{700}-crosslinked LCE5, with R_f dropping below 40%, compared to PEG_{250}-crosslinked LCE5, with R_f remaining above 60%. This is because the increased crosslinking density and loss of interactions between chains due

to disturbed LC domains hinder the ability of LCEs to maintain their temporary shape. Therefore, the material tends to revert more to its original shape after unloading, driven by its entropy. Then, as shown in Figure 4c, the addition of PEG diacrylates leads to a complete recovery before reaching 120 °C, in contrast to standard LCE5 which exhibits a recovery of 87% at 120 °C. Furthermore, the maximum recovery temperature values for all samples align with previous results, being close to the T_{NI} determined by DMA. In particular, adding PEG_{700} results in recovery at lower temperatures compared to PEG_{250}. This is because less energy is required to disrupt LC domains with PEG_{700}-crosslinked LCE5 compared to PEG_{250}-crosslinked LCE5.

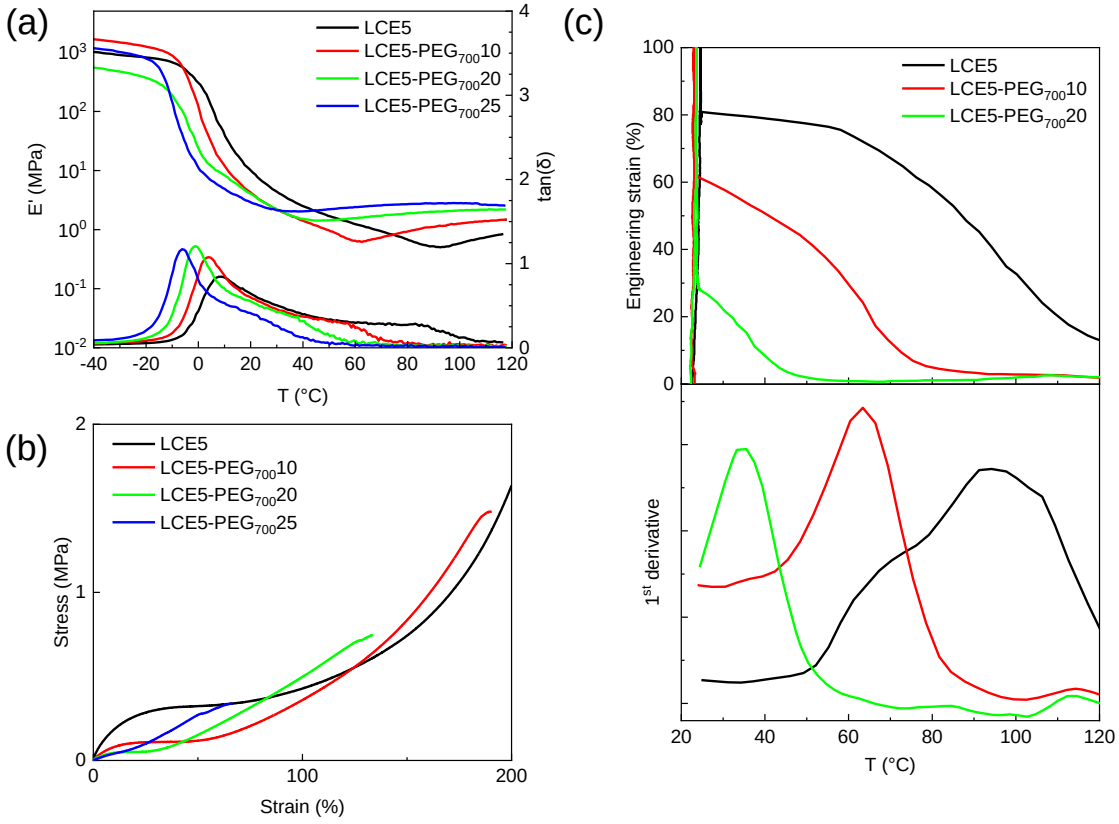

Figure 4: (a) Storage modulus (E') and loss tangent (tan δ) traces of PEG_{700}-crosslinked LCE5, labelled "LCE5"–"$PEG_{700}z$", *z* being the mole fraction of acrylate functional groups contributed by PEG_{700} to the network. (b) Stress–strain curves of PEG_{700}-crosslinked LCE5.

(c) Strain recovery behaviour and associated first derivative of the engineering strain as a function of temperature for PEG_{700}-crosslinked LCE5.

Table 3: Summary of DMA and tensile test data for PEG-crosslinked LCE5 characterization.

	T_g[a] (°C)	T_{NI}[a] (°C)	E'_n[a] (MPa)	E'_i[a] (MPa)	Young modulus[b] (MPa)	Threshold stress[b] (kPa)	Failure strain[b] (%)
LCE5-PEG_{250}20	18	74	10.9	0.9	5.9 ± 0.6	173.3 ± 16.7	260.6 ± 12.7
LCE5-PEG_{250}25	25	66	12.8	0.9	9.2 ± 1.9	200.8 ± 58.0	226.5 ± 4.4
LCE5-PEG_{250}45	42	69	57.0	1.9	22.1 ± 0.4	409.7 ± 71.8	207.1 ± 6.3
LCE5-PEG_{700}10	4	62	3.0	1.0	1.9 ± 0.3	69.8 ± 7.8	203.7 ± 11.9
LCE5-PEG_{700}20	-1	46	2.9	1.7	1.3 ± 0.1	38.8 ± 1.1	131.3 ± 2.6
LCE5-PEG_{700}25	-6	36	2.5	2.3	0.9 ± 0.1	25.1 ± 5.5	62.1 ± 4.1

[a] Determined by DMA. [b] Determined by uniaxial tensile testing.

We then examined in more detail the impact of these linkers on the LC order. POM was carried out on PEG_{250}-crosslinked LCE5 and PEG_{700}-crosslinked LCE5 to investigate the presence of LC order (Figure S11). POM images of these polydomain networks all show birefringent

regions known as Schlieren textures characteristic of LC order,[51] with no major differences observed with the addition of PEG_{250} and PEG_{700}. WAXS was conducted to assess how the incorporation of PEG diacrylates into LCE networks hinders the nematic order, thereby explaining the distinct properties observed such as lower T_{NI} (Figure 5 and Figure S12). WAXS analyses were performed to estimate the order parameters of PEG_{250}-crosslinked LCE5 and PEG_{700}-crosslinked LCE5 stretched to 30% engineering strain (excluding LCE5-PEG_{250}45 and LCE5-PEG_{700}25 for the same reasons above). The order parameter values at 25 °C and 65 °C are listed in Table 4. First, adding non-mesogenic linkers to the LCE networks results in a decrease in the order parameter at 25 °C, indicating a disrupted nematic order. The order parameter of LCE5 is 0.32, while PEG-crosslinked LCE5 samples show values of 0.25 or less. Then, increasing the molar content of non-mesogenic linkers accelerates the decrease in the order parameter with increasing temperature, with the networks reaching the isotropic state at lower temperatures (Figure 5c). Furthermore, PEG_{700} has a greater impact on disrupting the nematic order than PEG_{250}. For instance, when comparing LCE5-PEG_{250}20 and LCE5-PEG_{700}20 which have the same molar content of non-mesogenic linkers, the order parameter is slightly lower with PEG_{700} (0.22) than with PEG_{250} (0.25). At 65 °C, this difference becomes more pronounced, with values of 0.12 for PEG_{700} and 0.20 for PEG_{250}. This can be attributed to PEG_{700} introducing more mobility into the network due to its lower Tg, making mesogenic interactions even less favourable as the temperature inceases compared to PEG_{250}.

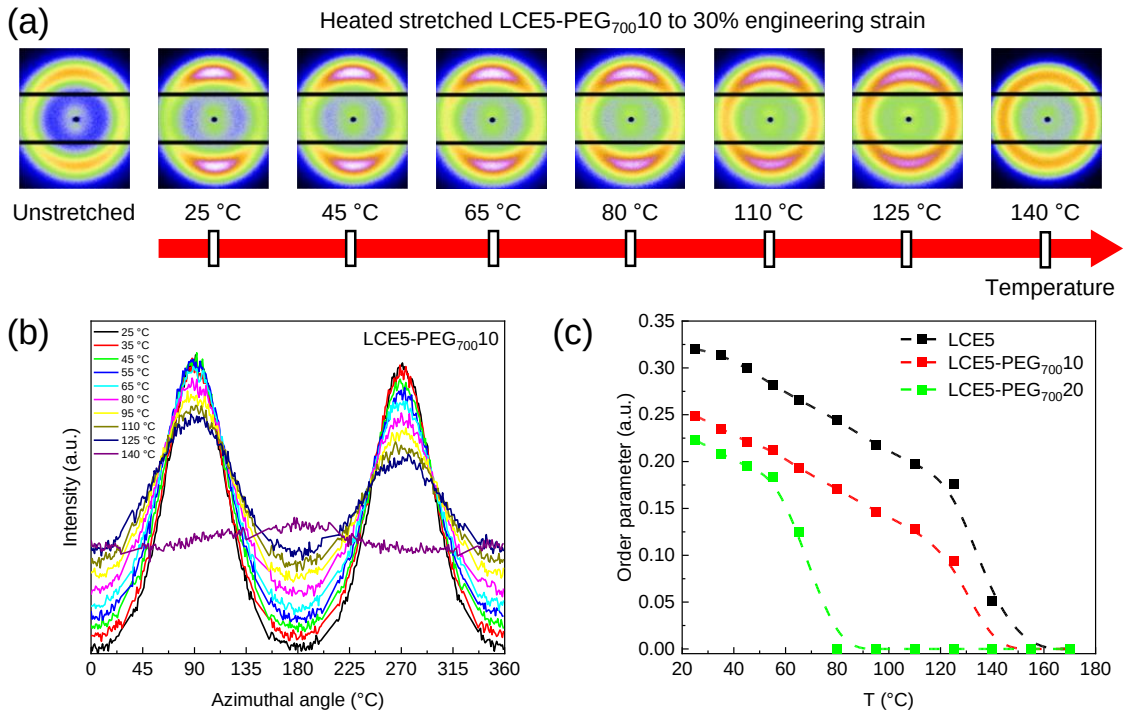

Figure 5: (a) 2D WAXS images of LCE5-PEG$_{700}$10 stretched to 30% engineering strain as a function of temperature. (b) WAXS azimuthal intensity distribution of LCE5-PEG$_{700}$10 stretched to 30% engineering strain as a function of temperature. (c) Evolution of order parameters for PEG$_{700}$-crosslinked LCE5 stretched to 30% engineering strain as a function of temperature. The dashed lines are guide to the eye.

Table 4: Summary of strain recovery testing and WAXS data for PEG-crosslinked LCE5 characterization.

	R_f[a] (%)	Stress at max. strain[a] (MPa)	Max. recovery temperature[a] (°C)	Order parameter at 25 °C[b]	Order parameter at 65 °C[b]
LCE5	81	0.17	94	0.32	0.27
LCE5-PEG$_{250}$20	72	0.33	86	0.25	0.20

LCE5-$PEG_{250}25$	61	0.54	74	0.24	0.20
LCE5-$PEG_{700}10$	62	0.17	63	0.25	0.19
LCE5-$PEG_{700}20$	28	0.32	36	0.22	0.12

[a] Determined by strain recovery testing. [b] Determined by WAXS.

Design and printing of shape-memory LCEs

The observed shape-memory behavior of LCEs was used to fabricate 3D structures with enhanced control over the shape recovery *via* the addition of non-mesogenic linkers. Two inks were formulated: one with only LCO5 and the other with a combination of LCO5 and PEG_{700}, so that 10 mol% of acrylate functional groups were contributed by PEG_{700} to the network. Orange G (0.2 wt%) was added to both resins as a light absorber to improve printing accuracy. These formulations were selected based on previous strain recovery results, with both LCE5 and LCE5-$PEG_{700}10$ networks demonstrating suitably high fixity. The same labels were kept for the DLP 3D printed networks from both inks. We first designed an artificial muscle-like structure mimicking muscle actions. This design resembles a muscle with the rods mimicking muscle fibers and allowing for extension and contraction movements. The artificial muscle-like structures were DLP 3D printed using both inks. They were subjected to uniaxial extension to 100% engineering strain which was calculated between the cylindrical top and bottom. Using the same reference marks, the structures exhibit a R_f of 72% for LCE5 and 67% for LCE5-$PEG_{700}10$. The structures were then immersed in a hot water bath. The LCE5 structure only fully recovers at 95 °C, while the LCE5-$PEG_{700}10$ recovers at 60 °C (Supplementary videos S1 and S2). These findings align with previous shape recovery results. We then designed a

stickman to demonstrate multiaxial stretching. The stickmen were DLP 3D printed using both inks with the same printing parameters as the artificial muscle-like structures. The body, legs, and arms of the stickman were extended to 100% engineering strain from one extremity to the other. The R_f values were close for both LCE networks (Table S1). The stickmen were then placed on a heating plate. As for the artificial muscle-like structures, LCE5 stickman fully recovers at 95 °C, while the LCE5-PEG$_{700}$10 stickman recovers at 60 °C (Supplementary videos S3 and S4). All these results indicate that tuning the properties of LCEs by adding non-mesogenic linkers of various lengths enables the fabrication of 3D printed soft actuators with controlled thermal and mechanical properties.

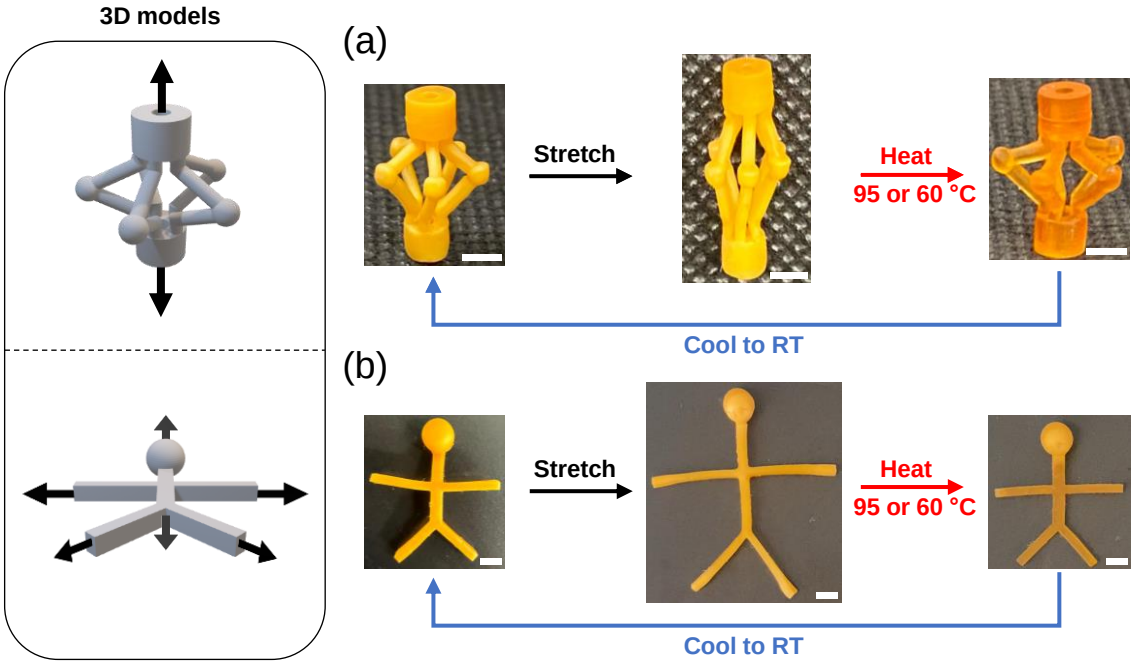

Figure 6: (a) Shape memory mechanism of a DLP printed artificial muscle-like LCE structure. The structure was subjected to uniaxial stretching, followed by heating at 95 °C and 60 °C for LCE5 and LCE5-PEG$_{700}$10 materials, respectively. (b) Shape memory mechanism of a DLP printed LCE stickman. The stickman was subjected to multiaxial stretching, followed by heating at 95 °C and 60 °C for LCE5 and LCE5-PEG$_{700}$10 materials, respectively. The white scale bars represent 0.5 cm.

CONCLUSIONS

In this study, we introduce a versatile method to tailor the thermo-mechanical properties of LCEs that can be DLP 3D printed in complex geometries. LCOs of different lengths are synthesised *via* a base-catalysed thiol-Michael polyaddition and are subsequently photo-crosslinked into LCEs under UV light. Control of the thermo-mechanical properties is achieved by adding non-mesogenic linkers of different lenghts such as PEG_{250} and PEG_{700}. The addition of these linkers is more pronounced as LCO length decreases. The addition of PEG_{250} increases the Tg and stiffness of LCEs, with moduli of up to 57 MPa, without having any significant impact on their failure strain. In contrast, the addition of PEG_{700} slightly decreases both Tg and stiffness, and significantly reduces the failure strain. The T_{NI} is also significantly influenced, with PEG_{700} causing a greater decrease than PEG_{250} down to 36 °C. These results are in agreement with shape recovery tests, with the addition of PEG_{700} also leading to a greater decrease in fixity than PEG_{250}. WAXS measurements indicate that non-mesogenic linkers hinder the nematic order of LCEs, with PEG_{700} having a greater impact than PEG_{250}. This presented method is successfully applied by DLP 3D printing structures as articifcal muscle-like objects and stickmen with enhanced control over the shape recovery *via* the addition of PEG_{700}. We believe that this approach paves new ways for 4D-printed soft actuators by offering a precise control of their properties in order to meet the needs of specific applications.

ASSOCIATED CONTENT

Appendix A. Supplementary material.

Supporting Information contains ^{1}H NMR spectra, gel fraction results, additional spectra and graphs from DMA, DSC thermogram, additional stress-strain curves, POM images, additional WAXS azimuthal intensity distribution spectra and an additional table of fixity values for 3D printed stickmen. The files are available free of charge.

CRediT authorship contribution statement

Rakine Mouhoubi: Conceptualization, Methodology, Investigation, Writing - Original Draft ; **Philippe Dieudonné-Georges**: Methodology, Formal analysis, Validation ; **Olivier Arnould**: Methodology, Formal analysis, Validation ; **Vincent Lapinte**: Supervision, Conceptualization, Writing - Review & Editing ; **Sébastien Blanquer:** Supervision, Conceptualization, Writing - Review & Editing, Project administration.

Corresponding Author

Sebastien Blanquer

E-mail: sebastien.blanquer@umontpellier.fr

Funding Sources

This work received financial support from the State, managed by the National Research Agency (ANR) under the France 2030 program, with reference ANR-21-RHUS-011.

Acknowledgment

The authors would like to thank the people from Laboratoire de Mécanique et Génie Civil (LMGC), Dr. Simon Le Floc'h and Dr. Cristina Cavinato for their help in the thermomechanical measurements.

Data availability

Data will be made available upon request.

REFERENCES

[1] I. Apsite, S. Salehi, L. Ionov, Materials for Smart Soft Actuator Systems, Chem. Rev. 122 (2022) 1349–1415. https://doi.org/10.1021/acs.chemrev.1c00453.

[2] Z.X. Khoo, J.E.M. Teoh, Y. Liu, C.K. Chua, S. Yang, J. An, K.F. Leong, W.Y. Yeong, 3D printing of smart materials: A review on recent progresses in 4D printing, Virtual and Physical Prototyping 10 (2015) 103–122. https://doi.org/10.1080/17452759.2015.1097054.

[3] E. Acome, S.K. Mitchell, T.G. Morrissey, M.B. Emmett, C. Benjamin, M. King, M. Radakovitz, C. Keplinger, Hydraulically amplified self-healing electrostatic actuators with muscle-like performance, Science 359 (2018) 61–65. https://doi.org/10.1126/science.aao6139.

[4] Q. He, Z. Wang, Y. Wang, A. Minori, M.T. Tolley, S. Cai, Electrically controlled liquid crystal elastomer–based soft tubular actuator with multimodal actuation, Sci. Adv. 5 (2019) eaax5746. https://doi.org/10.1126/sciadv.aax5746.

[5] M. Li, A. Pal, A. Aghakhani, A. Pena-Francesch, M. Sitti, Soft actuators for real-world applications, Nat Rev Mater 7 (2021) 235–249. https://doi.org/10.1038/s41578-021-00389-7.

[6] N. El-Atab, R.B. Mishra, F. Al-Modaf, L. Joharji, A.A. Alsharif, H. Alamoudi, M. Diaz, N. Qaiser, M.M. Hussain, Soft Actuators for Soft Robotic Applications: A Review, Advanced Intelligent Systems 2 (2020) 2000128. https://doi.org/10.1002/aisy.202000128.

[7] X. Kong, M. Dong, M. Du, J. Qian, J. Yin, Q. Zheng, Z.L. Wu, Recent Progress in 3D Printing of Polymer Materials as Soft Actuators and Robots, Chem Bio Eng. 1 (2024) 312–329. https://doi.org/10.1021/cbe.4c00028.

[8] F. Momeni, S. M.Mehdi Hassani.N, X. Liu, J. Ni, A review of 4D printing, Materials & Design 122 (2017) 42–79. https://doi.org/10.1016/j.matdes.2017.02.068.

[9] Q. Song, Y. Chen, V. Slesarenko, P. Zhu, A. Hamza, P. Hou, D. Helmer, F. Kotz-Helmer, B.E. Rapp, 4D Printed Shape-Memory Elastomer for Thermally Programmable Soft Actuators, ACS Appl. Mater. Interfaces 15 (2023) 40923–40932. https://doi.org/10.1021/acsami.3c07436.

[10] C.A. Spiegel, M. Hackner, V.P. Bothe, J.P. Spatz, E. Blasco, 4D Printing of Shape Memory Polymers: From Macro to Micro, Adv Funct Materials 32 (2022) 2110580. https://doi.org/10.1002/adfm.202110580.

[11] A. Subash, B. Kandasubramanian, 4D printing of shape memory polymers, European Polymer Journal 134 (2020) 109771. https://doi.org/10.1016/j.eurpolymj.2020.109771.

[12] T. Brossier, M. Habib, B.T. Benkhaled, G. Volpi, V. Lapinte, S. Blanquer, 4D printing of hydrogels based on poly(oxazoline) and poly(acrylamide) copolymers by stereolithography, Mater. Adv. 5 (2024) 2750–2758. https://doi.org/10.1039/D3MA00665D.

[13] J. Lai, X. Ye, J. Liu, C. Wang, J. Li, X. Wang, M. Ma, M. Wang, 4D printing of highly printable and shape morphing hydrogels composed of alginate and methylcellulose, Materials & Design 205 (2021) 109699. https://doi.org/10.1016/j.matdes.2021.109699.

[14] M. Champeau, D.A. Heinze, T.N. Viana, E.R. De Souza, A.C. Chinellato, S. Titotto, 4D Printing of Hydrogels: A Review, Adv Funct Materials 30 (2020) 1910606. https://doi.org/10.1002/adfm.201910606.

[15] B. Jin, J. Liu, Y. Shi, G. Chen, Q. Zhao, S. Yang, Solvent-Assisted 4D Programming and Reprogramming of Liquid Crystalline Organogels, Advanced Materials 34 (2022) 2107855. https://doi.org/10.1002/adma.202107855.

[16] M.O. Saed, C.P. Ambulo, H. Kim, R. De, V. Raval, K. Searles, D.A. Siddiqui, J.M.O. Cue, M.C. Stefan, M.R. Shankar, T.H. Ware, Molecularly-Engineered, 4D-Printed Liquid

Crystal Elastomer Actuators, Adv. Funct. Mater. 29 (2019) 1806412. https://doi.org/10.1002/adfm.201806412.

[17] D.J. Roach, X. Kuang, C. Yuan, K. Chen, H.J. Qi, Novel ink for ambient condition printing of liquid crystal elastomers for 4D printing, Smart Mater. Struct. 27 (2018) 125011. https://doi.org/10.1088/1361-665X/aae96f.

[18] L. McDougall, J. Herman, E. Huntley, S. Leguizamon, A. Cook, T. White, B. Kaehr, D.J. Roach, Free-Form Liquid Crystal Elastomers via Embedded 4D Printing, ACS Appl. Mater. Interfaces 15 (2023) 58897–58904. https://doi.org/10.1021/acsami.3c14783.

[19] Z. Guan, L. Wang, J. Bae, Advances in 4D printing of liquid crystalline elastomers: materials, techniques, and applications, Mater. Horiz. 9 (2022) 1825–1849. https://doi.org/10.1039/D2MH00232A.

[20] X. Peng, S. Wu, X. Sun, L. Yue, S.M. Montgomery, F. Demoly, K. Zhou, R.R. Zhao, H.J. Qi, 4D Printing of Freestanding Liquid Crystal Elastomers via Hybrid Additive Manufacturing, Advanced Materials 34 (2022) 2204890. https://doi.org/10.1002/adma.202204890.

[21] K.M. Herbert, H.E. Fowler, J.M. McCracken, K.R. Schlafmann, J.A. Koch, T.J. White, Synthesis and alignment of liquid crystalline elastomers, Nat Rev Mater 7 (2021) 23–38. https://doi.org/10.1038/s41578-021-00359-z.

[22] Md.A. Islam, L. Talukder, Md.F. Al, S.K. Sarker, S.M. Muyeen, P. Das, Md.M. Hasan, S.K. Das, Md.M. Islam, Md.R. Islam, S.I. Moyeen, F.R. Badal, Md.H. Ahamed, S.H. Abhi, A review on self-healing featured soft robotics, Front. Robot. AI 10 (2023) 1202584. https://doi.org/10.3389/frobt.2023.1202584.

[23] A. Kotikian, R.L. Truby, J.W. Boley, T.J. White, J.A. Lewis, 3D Printing of Liquid Crystal Elastomeric Actuators with Spatially Programed Nematic Order, Adv. Mater. 30 (2018) 1706164. https://doi.org/10.1002/adma.201706164.

[24] X. Song, W. Zhang, H. Liu, L. Zhao, Q. Chen, H. Tian, 3D printing of liquid crystal elastomers-based actuator for an inchworm-inspired crawling soft robot, Front. Robot. AI 9 (2022) 889848. https://doi.org/10.3389/frobt.2022.889848.

[25] Y. Wang, R. Yin, L. Jin, M. Liu, Y. Gao, J. Raney, S. Yang, 3D-Printed Photoresponsive Liquid Crystal Elastomer Composites for Free-Form Actuation, Adv Funct Materials 33 (2023) 2210614. https://doi.org/10.1002/adfm.202210614.

[26] J. Choi, Y. Choi, J. Lee, M.C. Kim, S. Park, K. Hyun, K.M. Lee, T. Yoon, S. Ahn, Direct-Ink-Written Cholesteric Liquid Crystal Elastomer with Programmable Mechanochromic Response, Adv Funct Materials (2023) 2310658. https://doi.org/10.1002/adfm.202310658.

[27] C.P. Ambulo, J.J. Burroughs, J.M. Boothby, H. Kim, M.R. Shankar, T.H. Ware, Four-dimensional Printing of Liquid Crystal Elastomers, ACS Appl. Mater. Interfaces 9 (2017) 37332–37339. https://doi.org/10.1021/acsami.7b11851.

[28] S. Li, Z. Song, Y. Fan, D. Wei, Y. Liu, Four-Dimensional Printing of Temperature-Responsive Liquid Crystal Elastomers with Programmable Shape-Changing Behavior, Biomimetics 8 (2023) 196. https://doi.org/10.3390/biomimetics8020196.

[29] W. Qiu, X. He, Z. Fang, Y. Wang, K. Dong, G. Zhang, X. Xu, Q. Ge, Y. Xiong, Shape-Tunable 4D Printing of LCEs via Cooling Rate Modulation: Stimulus-Free Locking of

Actuated State at Room Temperature, ACS Appl. Mater. Interfaces 15 (2023) 47509–47519. https://doi.org/10.1021/acsami.3c10210.

[30] Z. Wang, Z. Wang, Y. Zheng, Q. He, Y. Wang, S. Cai, Three-dimensional printing of functionally graded liquid crystal elastomer, Sci. Adv. 6 (2020) eabc0034. https://doi.org/10.1126/sciadv.abc0034.

[31] S. Gantenbein, K. Masania, W. Woigk, J.P.W. Sesseg, T.A. Tervoort, A.R. Studart, Three-dimensional printing of hierarchical liquid-crystal-polymer structures, Nature 561 (2018) 226–230. https://doi.org/10.1038/s41586-018-0474-7.

[32] P. Mainik, L. Hsu, C.W. Zimmer, D. Fauser, H. Steeb, E. Blasco, DLP 4D Printing of Multi-Responsive Bilayered Structures, Adv Materials Technologies (2023) 2300727. https://doi.org/10.1002/admt.202300727.

[33] S. Li, H. Bai, Z. Liu, X. Zhang, C. Huang, L.W. Wiesner, M. Silberstein, R.F. Shepherd, Digital light processing of liquid crystal elastomers for self-sensing artificial muscles, Sci. Adv. 7 (2021) eabg3677. https://doi.org/10.1126/sciadv.abg3677.

[34] G. Chen, B. Jin, Y. Shi, Q. Zhao, Y. Shen, T. Xie, Rapidly and Repeatedly Reprogrammable Liquid Crystalline Elastomer via a Shape Memory Mechanism, Advanced Materials 34 (2022) 2201679. https://doi.org/10.1002/adma.202201679.

[35] M. Tabrizi, T.H. Ware, M.R. Shankar, Voxelated Molecular Patterning in Three-Dimensional Freeforms, ACS Appl. Mater. Interfaces 11 (2019) 28236–28245. https://doi.org/10.1021/acsami.9b04480.

[36] N.A. Traugutt, D. Mistry, C. Luo, K. Yu, Q. Ge, C.M. Yakacki, Liquid-Crystal-Elastomer-Based Dissipative Structures by Digital Light Processing 3D Printing, Adv. Mater. 32 (2020) 2000797. https://doi.org/10.1002/adma.202000797.

[37] O.M. Wani, H. Zeng, P. Wasylczyk, A. Priimagi, Programming Photoresponse in Liquid Crystal Polymer Actuators with Laser Projector, Advanced Optical Materials 6 (2018) 1700949. https://doi.org/10.1002/adom.201700949.

[38] G.E. Bauman, J.M. McCracken, T.J. White, Actuation of Liquid Crystalline Elastomers at or Below Ambient Temperature, Angew Chem Int Ed 61 (2022). https://doi.org/10.1002/anie.202202577.

[39] Z.-C. Jiang, Q. Liu, Y.-Y. Xiao, Y. Zhao, Liquid crystal elastomers for actuation: A perspective on structure-property-function relation, Progress in Polymer Science 153 (2024) 101829. https://doi.org/10.1016/j.progpolymsci.2024.101829.

[40] R.K. Shaha, A.H. Torbati, C.P. Frick, Body-temperature shape shifting liquid crystal elastomers, J Appl Polym Sci 138 (2021) 50136. https://doi.org/10.1002/app.50136.

[41] Y. Zhan, D.J. Broer, J. Li, J. Xue, D. Liu, A cold-responsive liquid crystal elastomer provides visual signals for monitoring a critical temperature decrease, Mater. Horiz. (2023) 10.1039.D3MH00271C. https://doi.org/10.1039/D3MH00271C.

[42] H. Kim, J.M. Boothby, S. Ramachandran, C.D. Lee, T.H. Ware, Tough, Shape-Changing Materials: Crystallized Liquid Crystal Elastomers, Macromolecules 50 (2017) 4267–4275. https://doi.org/10.1021/acs.macromol.7b00567.

[43] M.O. Saed, R.H. Volpe, N.A. Traugutt, R. Visvanathan, N.A. Clark, C.M. Yakacki, High strain actuation liquid crystal elastomers via modulation of mesophase structure, Soft Matter 13 (2017) 7537–7547. https://doi.org/10.1039/C7SM01380A.

[44] J. Bennett, Measuring UV curing parameters of commercial photopolymers used in additive manufacturing, Additive Manufacturing 18 (2017) 203–212. https://doi.org/10.1016/j.addma.2017.10.009.

[45] J. S. Bello Forero, J. A. Hernández Muñoz, J. Jones Junior, F. M. Da Silva, Propylene Carbonate in Organic Synthesis: Exploring its Potential as a Green Solvent, COS 13 (2016) 834–846. https://doi.org/10.2174/1570179413999160211094705.

[46] W.H. Carothers, Polymers and polyfunctionality, Transactions of the Faraday Society 32 (1936) 39–49.

[47] N.A. Traugutt, R.H. Volpe, M.S. Bollinger, M.O. Saed, A.H. Torbati, K. Yu, N. Dadivanyan, C.M. Yakacki, Liquid-crystal order during synthesis affects main-chain liquid-crystal elastomer behavior, Soft Matter 13 (2017) 7013–7025. https://doi.org/10.1039/C7SM01405H.

[48] D.R. Merkel, N.A. Traugutt, R. Visvanathan, C.M. Yakacki, C.P. Frick, Thermomechanical properties of monodomain nematic main-chain liquid crystal elastomers, Soft Matter 14 (2018) 6024–6036. https://doi.org/10.1039/C8SM01178H.

[49] M.O. Saed, A.H. Torbati, C.A. Starr, R. Visvanathan, N.A. Clark, C.M. Yakacki, Thiol-acrylate main-chain liquid-crystalline elastomers with tunable thermomechanical properties and actuation strain, J. Polym. Sci. Part B: Polym. Phys. 55 (2017) 157–168. https://doi.org/10.1002/polb.24249.

[50] M. Barnes, S. Cetinkaya, A. Ajnsztajn, R. Verduzco, Understanding the effect of liquid crystal content on the phase behavior and mechanical properties of liquid crystal elastomers, Soft Matter 18 (2022) 5074–5081. https://doi.org/10.1039/D2SM00480A.

[51] J. Nehring, A. Saupe, On the schlieren texture in nematic and smectic liquid crystals, J. Chem. Soc., Faraday Trans. 2 68 (1972) 1. https://doi.org/10.1039/f29726800001.